McKay, R.M., De Santis, L., Kulhanek, D.K., and the Expedition 374 Scientists
Proceedings of the International Ocean Discovery Program Volume 374
publications.iodp.org

Data report: sedimentary X-ray fluorescence scanning of International Ocean Discovery Program Expedition 374 Site U1521, Ross Sea, Antarctica[1]

Imogen M. Browne,[2] Amelia E. Shevenell,[2] Catherine Prunella,[3, 4] Denise K. Kulhanek,[2] and the Expedition 374 Scientists[2]

[1] Browne, I.M., Shevenell, A.E., Prunella, C., Kulhanek, D.K., and the Expedition 374 Scientists, 2026. Data report: sedimentary X-ray fluorescence scanning of International Ocean Discovery Program Expedition 374 Site U1521, Ross Sea, Antarctica. In McKay, R.M., De Santis, L., Kulhanek, D.K., and the Expedition 374 Scientists, Ross Sea West Antarctic Ice Sheet History. Proceedings of the International Ocean Discovery Program, 374: College Station, TX (International Ocean Discovery Program). https://doi.org/10.14379/iodp.proc.374.204.2026
[2] **Expedition 374 Scientists' affiliations.** Correspondence author: **ibrowne@binghamton.edu**
[3] College of Marine Science, University of South Florida, USA.
[4] New York Sea Grant, National Ocean and Atmospheric Administration, USA.

Keywords
International Ocean Discovery Program, IODP, *JOIDES Resolution*, Expedition 374, Ross Sea West Antarctic Ice Sheet History, Site U1521, Miocene, X-ray fluorescence, XRF, glaciomarine sediments

Supplementary material

References (RIS)

MS 374-204
Received 12 September 2025
Accepted 11 December 2025
Published 7 April 2026

Abstract

Marine sediment cores from ice-proximal locations enable reconstructions of Antarctic environmental change and ice sheet evolution. Here, we report semiquantitative X-ray fluorescence (XRF) core scanning results from ~650 m of glaciomarine sediments recovered during International Ocean Discovery Program Expedition 374 from Site U1521, located on the middle to outer Ross Sea continental shelf. Raw XRF data were scaled using shipboard inductively coupled plasma–optical emission spectroscopy (ICP-OES), normalized, and then considered in the context of Site U1521 lithologic data. We find that diamictites have higher relative amounts of lithogenic elements (e.g., Ti, K, and Fe), whereas diatom-rich intervals have higher relative amounts of elements traditionally associated with biogenic productivity (e.g., Si and Br). These XRF data can be used in future studies to reconstruct a range of sedimentary and oceanographic processes that will provide insight into the evolution of the West Antarctic Ice Sheet.

1. Introduction

International Ocean Discovery Program (IODP) Expedition 374 drilled Site U1521 (75°41.0′S, 179°40.3′W; 562 m water depth) on the middle to outer continental shelf in the Pennell Basin, Ross Sea (Figure **F1**), to test hypotheses related to Neogene evolution of the West Antarctic Ice Sheet, particularly in the Miocene (**McKay et al.**, 2019a). Site U1521 was drilled to a total depth of 650.1 meters below seafloor (mbsf) and recovered 411.5 m (63% recovery) of Lower Miocene to Pleistocene sediments. The sedimentary sequence includes seven lithostratigraphic units (**McKay et al.**, 2019b) containing diamictites, mudstones, diatom-rich mudstones, and diatomites that provide insight into past depositional environments (Marschalek et al., 2021; Pérez et al., 2022; McKay et al., 2024).

X-ray fluorescence (XRF) core scanning of Site U1521 sediments provides semiquantitative data useful for further characterizing sedimentary units, as well as for paleoceanographic and terrigenous provenance studies (e.g., Grützner et al., 2003; Monien et al., 2012; Cook et al., 2013; Patterson et al., 2014; Croudace and Rothwell, 2015; Bertram et al., 2018; Penkrot et al., 2018; Wilson et al., 2018; Jimenez-Espejo et al., 2020). Here, we report XRF data from Site U1521. Raw XRF counts are influenced by sediment density and atomic weight (e.g., Tjallingii et al., 2007; Lyle et al., 2012; Kasuya et al., 2023) such that elements with higher atomic weights (e.g., Fe and Ba) emit higher energy X-rays compared to elements with lower atomic weights (e.g., Al and Si), resulting in attenuation of signals for elements with lower atomic weights (Tjallingii et al., 2007). To account for these effects, XRF data were (1) scaled to the median elemental concentrations of sediment collected from Site U1521, which were measured shipboard using inductively coupled plasma–optical emission spectroscopy (ICP-OES) to transform peak areas to weight percents and (2) normalized to eliminate variations caused by changes in sediment density, porosity, and cracking (Lyle et al., 2012). Normalized median-scaled (NMS_c) XRF data are plotted against shipboard lithology and natural gamma radiation (NGR), which reflects relative amounts of fine-grained terrigenous sediment (clays) (Figure **F2**) (**McKay et al.**, 2019b; Blum, 1997).

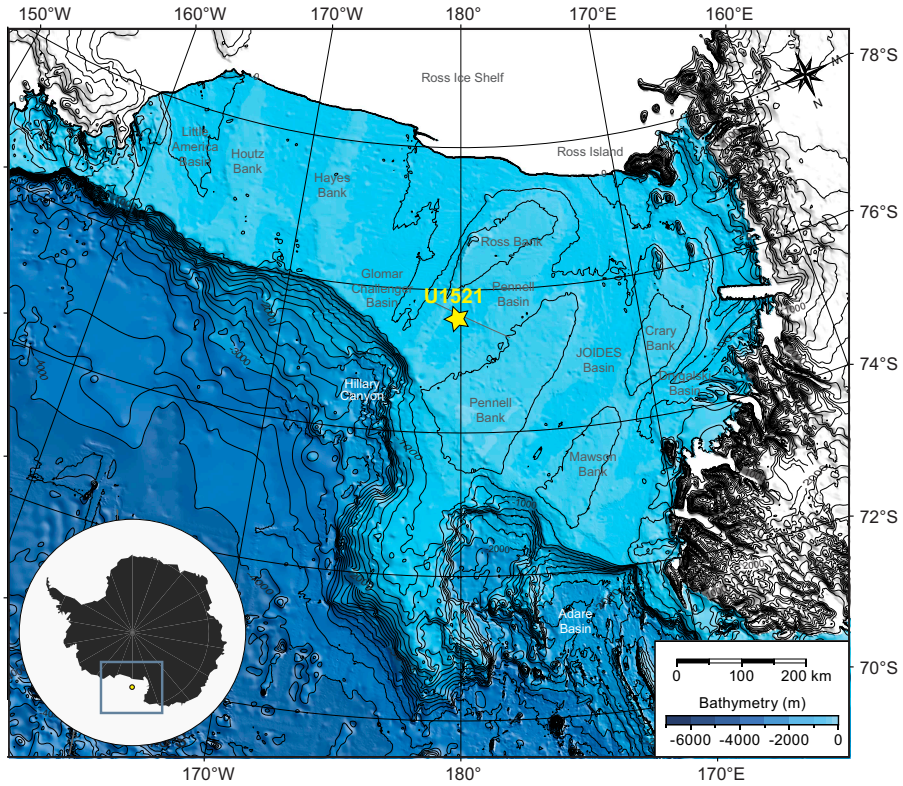

Figure F1. Map of the Ross Sea showing the location of Site U1521 in the Pennell Basin (yellow star). Modified from McKay et al. (2019a).

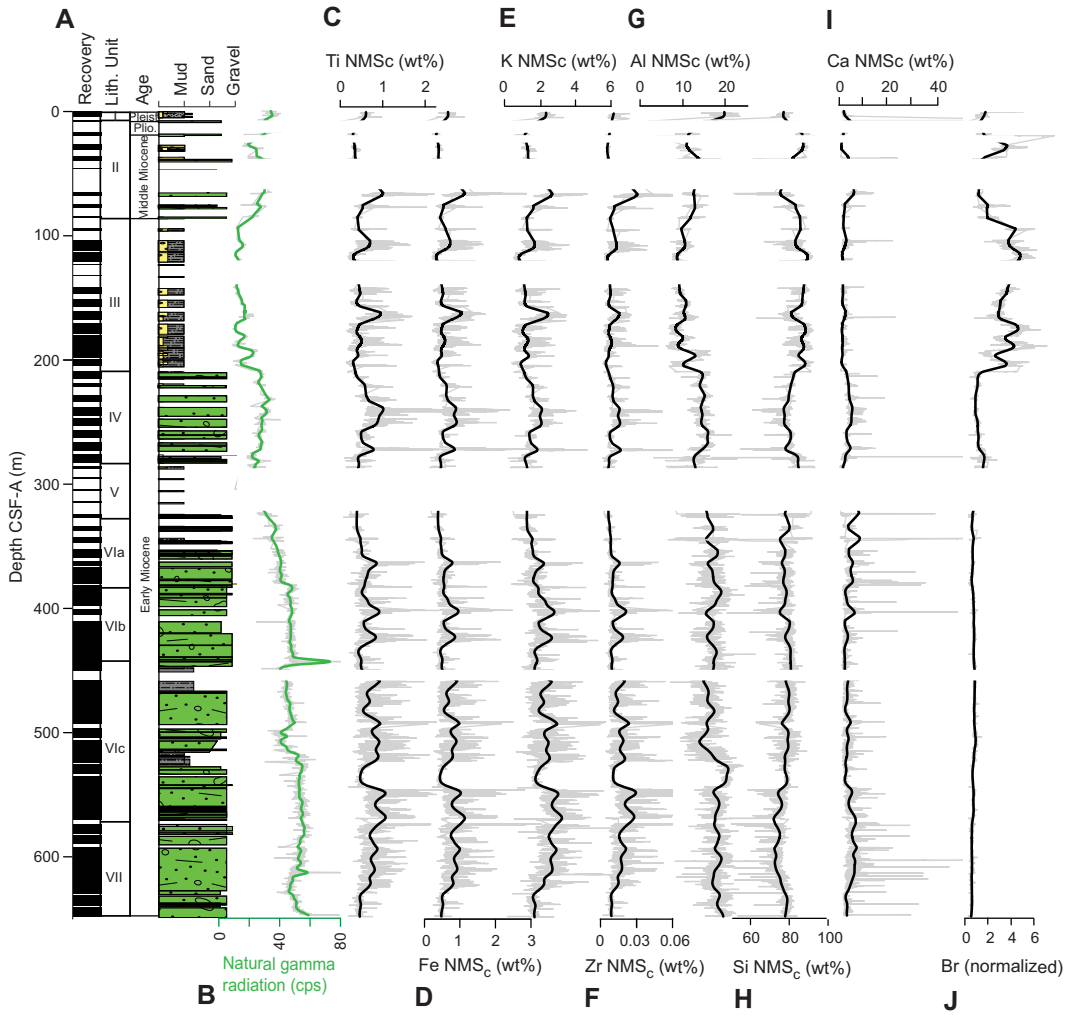

Figure F2. Lithology, NGR, and NMS_c XRF data from selected elements with depth, Site U1521. Ti, Fe, K, Al, Si, and Ca are from the 10kV scan, and Zr and Br are from the 30kV scan. CSF-A = core composite depth below seafloor, Method A; cps = counts per second.

2. Methods and materials

2.1. X-ray fluorescence scanning

XRF scanning was conducted on Site U1521 cores using a fourth generation Avaatech core scanner (designated XRF2) at the IODP Gulf Coast Repository in College Station, Texas (USA), following methods described in **Kulhanek et al.** (2022), which we outline in brief here. Core sections were removed from refrigeration at least 3 h prior to scanning to avoid condensation. Surfaces were lightly cleaned using a metal spatula to provide a fresh surface and then covered with 4 µm thick Ultralene film (SPEX Centriprep, Inc.) to protect the sensor. Each archive section half was scanned at 1 cm resolution using a 1.2 cm^2 illumination window set at 1 cm downcore and 1.2 cm crosscore. The cores were scanned at three excitation levels:10kV (6 s count time; 0.16 mA current; no filter) for major and minor elements (e.g., Al, Si, K, Ca, Ti, Mn, and Fe), 30 kV (6 s count time; 1.25 mA current; with a Pd-thick filter) for heavier major and minor elements and relevant trace elements (e.g., Ni, Sr, Rb, and Zr), and 50 kV (10 s count time; 0.75 mA current; with a Cu filter) for heavier trace elements (e.g., Ba). Obvious voids and cracks were skipped during scanning. Raw XRF data are archived in the IODP Zenodo database (**https://zenodo.org/records/7850848**).

2.2. Quality control

Raw spectra were processed into peak areas using bAxil XRF spectral processing software (Brightspec), which uses a nonlinear least squares method. Raw data with positive argon (Ar) values in the 10 kV scan were removed (n = 1245; 9% of all data) because such values indicate poor sensor contact with the core surface or the presence of small cracks that were not skipped (e.g., Dunlea et al., 2020). In the remaining data, no throughput values from the 10 kV scan were less than 150,000 counts/s (Robustelli Test et al., 2024). Depths with discrete peaks of Ca, Mn, Fe, Sr, and Ti were not removed from the data set because of associations with clasts and/or biogenic/authigenic carbonate (Figure **F3**). Quality controlled Site U1521 XRF data can be found in XRF in **Supplementary material**.

2.3. Scaling X-ray fluorescence data to shipboard elemental data

We scaled peak areas to typical site-specific sedimentologic compositions (e.g., diamictite, mudstone, and diatom-bearing to rich mudstones) by scaling raw median peak areas of each element to the median bulk sediment elemental concentrations, measured shipboard using ICP-OES (n = 16; Table **T1**) (**McKay et al.**, 2019b; Lyle et al., 2012). The sedimentary components are assumed to be Al_2O_3, $BaSO_4$, $CaCO_3$, FeO, K_2O, MgO, MnO, Na_2O, SiO_2, SrO, TiO_2, and ZrO_2 following Lyle et al. (2012). Briefly, elemental weight percents obtained using ICP-OES were converted to the equivalent oxide/carbonate weight proportion by multiplying the weight percent of the element obtained using ICP-OES by the molecular weight of the oxide/carbonate equivalent and dividing this value by the molecular weight of the cation. Oxide/carbonate weight proportions were then summed and normalized to 100% to obtain oxide/carbonate weight percents (Table **T1**). Scaling was completed using the converted oxide/carbonate weight percent using the following equation from Lyle et al. (2012):

$$S_e = \text{Median}\%_e \times \frac{\text{Peak Area}_e}{\text{Median Peak Area}_e},$$

where S_e is the scaled elemental value (in weight percent), $\text{Median}\%_e$ is the median weight percent of the most probable sedimentary component for each element (e.g., oxide and carbonate; Table **T1**), Peak Area_e is the peak area of an element from the scanned depth, and $\text{Median Peak Area}_e$ is the median of peak areas across all depths for that element.

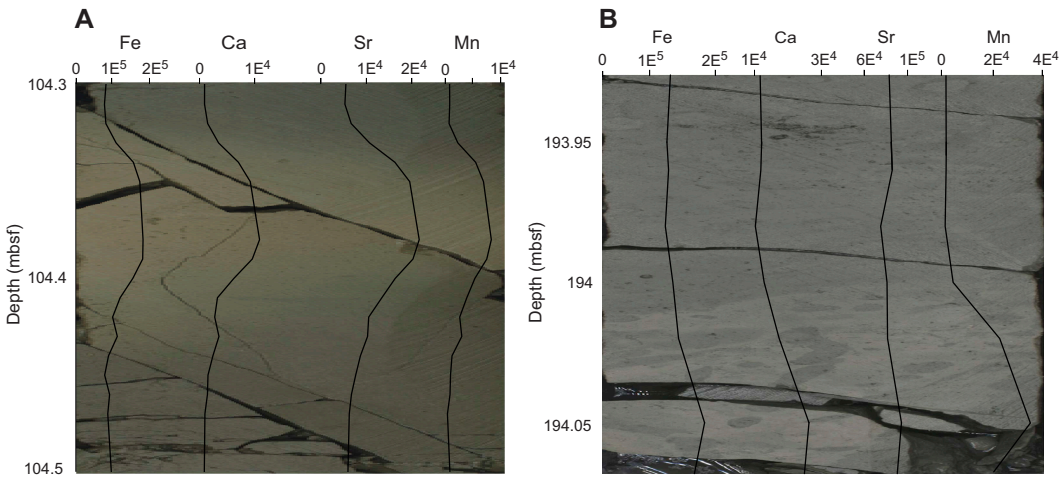

Figure F3. Changes in Fe, Ca, Sr, and Mn in (A) diatom-rich mudstone and (B) diatom-bearing mudstone. Elemental data associated with a color change related to authigenic carbonate presence.

Table T1. Shipboard bulk sedimentary geochemistry converted for oxides and carbonate, Site U1521. **Download table in CSV format.**

For elements measured in multiple scans (e.g., K at 10 and 30 kV and Ca at 10, 30, and 50 kV), scans with the highest peak area were used for scaling. Because Br and Ni in the 30 kV scan were not quantified using ICP-OES, these elements were not scaled.

2.4. Normalization of scaled data

To minimize variability introduced by porosity differences or cracks, scaled data were summed and normalized to 100% using the following equation (Lyle et al., 2012):

$$\mathrm{NMS}_c = \mathrm{C} \times \frac{100}{\text{sum of scaled elements}},$$

where NMS_c is the normalized median-scaled value for the element, C is the median scaled value of the element, and sum of scaled elements is the sum of all scaled elements at that depth.

2.5. Statistical analyses

To investigate the relationships among elements, we use both crossplots (Figures **F4**, **F5**) and correlation analysis (Figures **F6**, **F7**). Because the raw and NMS_c XRF data are not normally distributed, we conducted a Spearman's rank correlation to determine the strength and direction of correlations between element pairs (Figures **F5**, **F7**). The strength of the relationship between elements is quantified with the Spearman's rank correlation coefficient (ρ) and the strongest relationships between elements have a $\rho > 0.7$. Correlation analyses were performed using the *cor* function and plotted using the *corrplot* package in R (Figures **F5**, **F7**) (Wei and Simko, 2024; R Core Team, 2024).

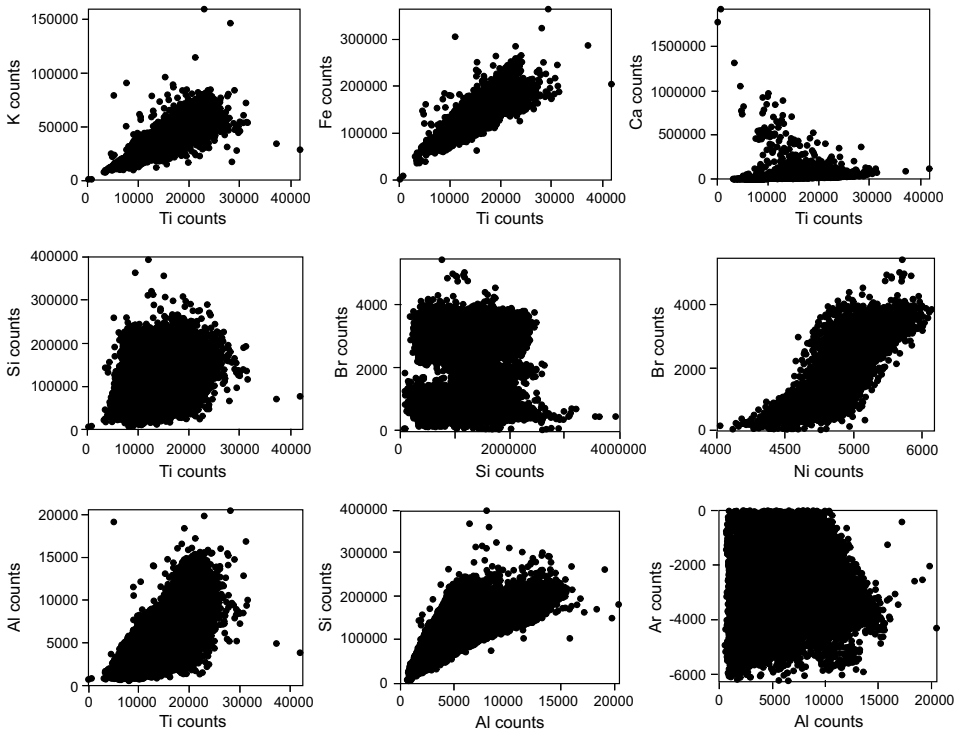

Figure F4. Crossplots of raw XRF data, Site U1521. Plots were made using RStudio (R Core Team, 2024).

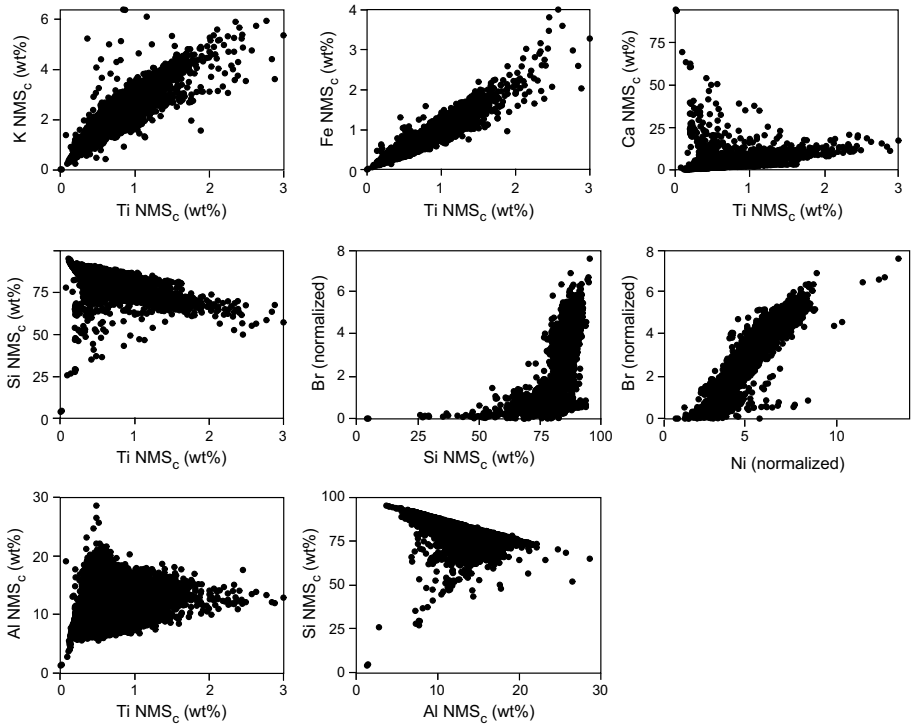

Figure F5. Crossplots of scaled and NMS$_c$ XRF data, Site U1521. Plots were made using RStudio (R Core Team, 2024).

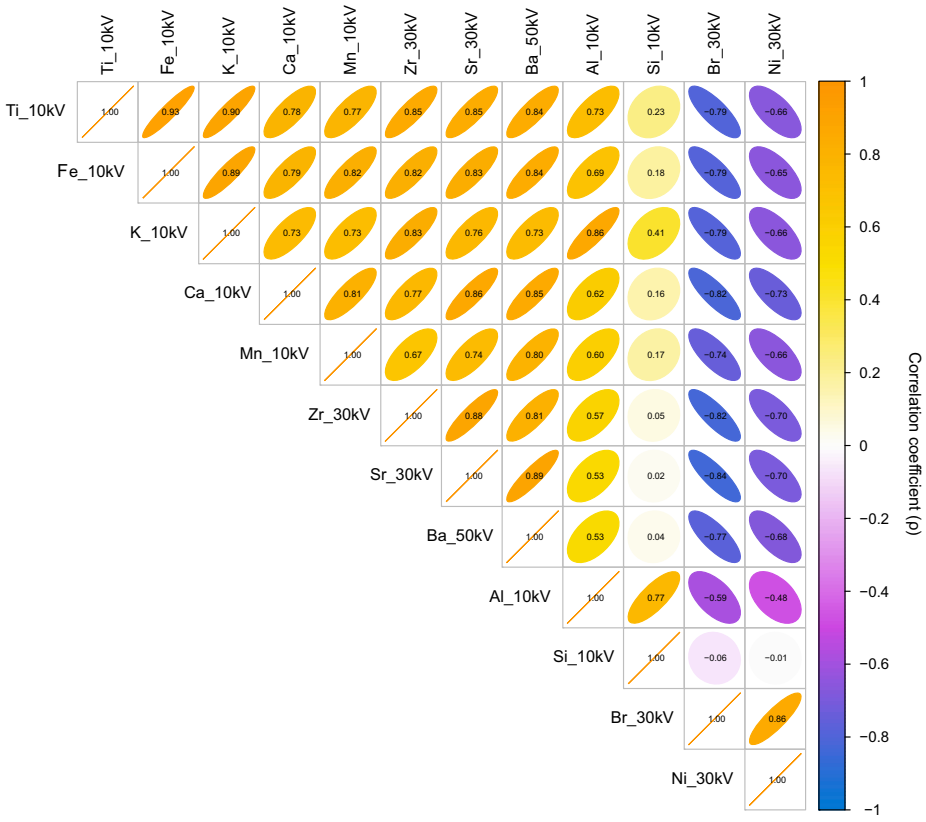

Figure F6. Correlogram of raw elements, Site U1521. Correlation between elements was determined by a Spearman's rank correlation. Correlation is shown on a color gradient from orange to blue (orange = positive correlation, blue = negative correlation). Yellow to purple colors indicate weak positive to negative correlations. The more elliptical the shape in the correlogram, the more correlated the elements are; the more spherical the shape, the less correlated. The correlation coefficient, ρ, for each correlation is shown on the ellipses. Strong correlations are considered to be those where ρ > 0.7. Plot was made following Wei and Simko (2024) using RStudio (R Core Team, 2024).

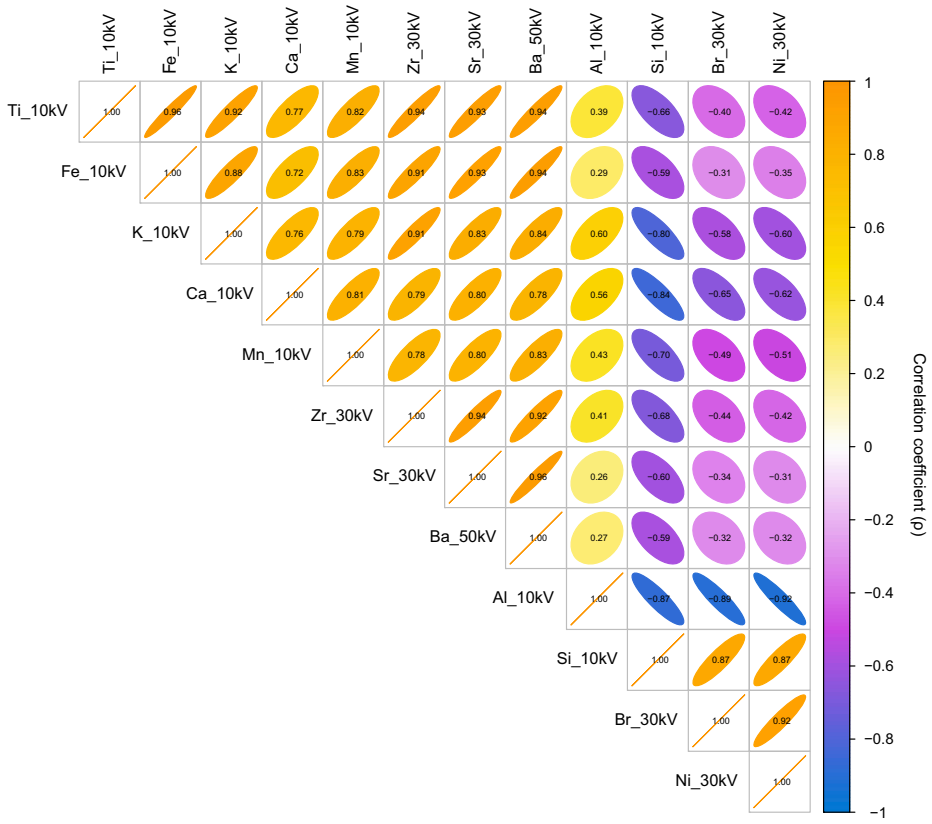

Figure F7. Correlogram of NMS_c elements, Site U1521. Correlation between elements was determined by a Spearman's rank correlation. Correlation is shown on a color gradient from orange to blue (orange = positive correlation, blue = negative correlation). Yellow to purple colors indicate weak positive to negative correlations. The more elliptical the shape in the correlogram, the more correlated the elements are; the more spherical the shape, the less correlated. The correlation coefficient, ρ, for each correlation is shown on the ellipses. Strong correlations are considered to be those where $\rho > 0.7$. Plot was made following Wei and Simko (2024) using RStudio (R Core Team, 2024).

3. Results

3.1. Relationships and correlation between elements

To verify relationships and correlations between elements commonly associated with terrigenous or biogenic sources at Site U1521 (e.g., Croudace and Rothwell, 2015; Gäng et al., 2023; Ziegler et al., 2008), we plotted raw elements against each other (Figure **F4**) and conducted a Spearman's rank correlation with raw elements (Figure **F6**). We find positive relationships and strong positive correlations ($\rho > 0.7$) between terrigenous elements (e.g., Ti and K, Ti and Fe, and Ti and Al) and between biogenic elements (e.g., Br and Ni). We observe negative relationships and moderate to strong negative correlations between terrigenous and biogenic elements (e.g., Ti and Br and Ti and Ni). Ca, which can have terrigenous, biogenic, and authigenic sources (Calvert and Pedersen, 2007; Croudace and Rothwell, 2015), shows a bimodal relationship with Ti (predominately lithogenic), suggesting that Ca has multiple sources at Site U1521. Si, which can have terrigenous or biogenic sources (Calvert and Pedersen, 2007; Croudace and Rothwell, 2015), shows no relationship or significant correlation with Ti but does show a positive relationship and high positive correlation ($\rho = 0.77$) with Al.

To investigate how normalizing and scaling influences relationships and correlations between elements, we plotted NMS_c elements with each other (Figure **F5**) and conducted a Spearman's rank correlation with NMS_c elements (Figure **F7**). We still find positive relationships and strong positive correlations ($\rho > 0.7$) between terrigenous elements (e.g., Ti and K and Ti and Fe) and between biogenic elements (e.g., Br and Ni) and negative relationships and correlations between terrigenous and biogenic elements (e.g., Ti and Br). However, the normalizing and scaling method

Table T2. Mean and maximum values for selected elements for diamictites and diatomites, Site U1521. **Download table in CSV format.**

changes the relationships of Si and Al with other elements. The relationship between Si and terrigenous elements becomes negative with moderate to strong negative correlation (e.g., Si and Ti and Si and K), and the relationship and correlation between Si and biogenic elements become positive with strong positive correlations (e.g., Si and Br and Si and Ni). This indicates that in some lithologies, such as the diatomites and diatom-rich mudstones, Si is predominately a biogenic element. The relationship and correlations between Al and terrigenous elements become weaker, suggesting that the source of Al is complicated at Site U1521. Overall, we demonstrate that normalizing and scaling the XRF data at Site U1521 helps to correct the lighter elements Si and Al for attenuation of the signal.

3.2. Stratigraphic trends

Downhole elemental variability corresponds to changes in sediment composition through time (Figure **F2**). Diamictites in Units I, II, IV, VI, and VII are characterized by higher NGR values (McKay et al., 2024). Lithogenic elements, including Ti, Fe, K, and Zr, have the highest maximum and mean values in diamictite lithologies (Table **T2**). Biogenic-associated elements, including Si and Br, have the highest mean values in diatom-bearing to diatom-rich mudstones (Table **T2**). In the lower part of Unit III, variations in NGR and Br indicate changes in the relative amounts of lithogenic and biogenic sediment. Finally, large peaks in Mn, Ca, and Sr in all units correspond with authigenic carbonates (Figures **F3**, **F2I**; Blanchet et al., 2007; Croudace and Rothwell, 2015).

4. Acknowledgments

This research was funded by NSF award PLR-1947646 to A.E. Shevenell and US Science Support funding to A.E. Shevenell and I.M. Browne. I.M. Browne was supported by an internal University of South Florida College of Marine Science fellowship. This research used samples and data provided by IODP. We thank the IODP Expedition 374 Scientists, technicians, crew, and the staff of the Gulf Coast Repository. We also thank Claudio Robustelli Test and Thomas Ronge for their insightful reviews, which helped improve this data report.

References

Bertram, R.A., Wilson, D.J., van de Flierdt, T., McKay, R.M., Patterson, M.O., Jimenez-Espejo, F.J., Escutia, C., Duke, G.C., Taylor-Silva, B.I., and Riesselman, C.R., 2018. Pliocene deglacial event timelines and the biogeochemical response offshore Wilkes subglacial basin, East Antarctica. Earth and Planetary Science Letters, 494:109–116. **https://doi.org/10.1016/j.epsl.2018.04.054**

Blanchet, C.L., Thouveny, N., Vidal, L., Leduc, G., Tachikawa, K., Bard, E., and Beaufort, L., 2007. Terrigenous input response to glacial/interglacial climatic variations over southern Baja California: a rock magnetic approach. Quaternary Science Reviews, 26(25):3118–3133. **https://doi.org/10.1016/j.quascirev.2007.07.008**

Blum, P., 1997. Technical Note 26: Physical properties handbook. Ocean Drilling Program. **https://doi.org/10.2973/odp.tn.26.1997**

Browne, I.M., Shevenell, A.E., Prunella, C., Kulhanek, D.K., and the Expedition 374 Scientists, 2026. Supplementary material, **https://doi.org/10.14379/iodp.proc.374.204supp.2026**. In Browne, I.M., Shevenell, A.E., Prunella, C., Kulhanek, D.K., and the Expedition 374 Scientists, Data report: sedimentary X-ray fluorescence scanning of International Ocean Discovery Program Expedition 374 Site U1521, Ross Sea, Antarctica. In McKay, R.M., De Santis, L., Kulhanek, D.K., and the Expedition 374 Scientists, Ross Sea West Antarctic Ice Sheet History. Proceedings of the International Ocean Discovery Program, 374: College Station, TX (International Ocean Discovery Program).

Calvert, S.E., and Pedersen, T.F., 2007. Elemental proxies for palaeoclimatic and palaeoceanographic variability in marine sediments: interpretation and application. In Hillaire–Marcel, C., and De Vernal, A. (Eds.), Developments in Marine Geology. 1: (Elsevier), 567–644. **https://doi.org/10.1016/S1572-5480(07)01019-6**

Cook, C.P., van de Flierdt, T., Williams, T., Hemming, S.R., Iwai, M., Kobayashi, M., Jimenez-Espejo, F.J., Escutia, C., González, J.J., Khim, B.-K., McKay, R.M., Passchier, S., Bohaty, S.M., Risselman, C.R., Tauxe, L., Sugisaki, S., Galindo, A.L., Patterson, M.O., Sangiorgi, F., Pierce, E.L., Brinkhuis, H., Klaus, A., Fehr, A., Bendle, J.A.P., Bijl, P.K., Carr, S.A., Dunbar, R.B., Flores, J.A., Hayden, T.G., Katsuki, K., Kong, G.S., Nakai, M., Olney, M.P., Pekar, S.F., Pross, J., Röhl, U., Sakai, T., Shrivastava, P.K., Stickley, C.E., Shouting, T., Welsh, K., and Yamane, M., 2013. Dynamic behaviour of the East Antarctic ice sheet during Pliocene warmth. Nature Geoscience, 6(9):765–769. **https://doi.org/10.1038/ngeo1889**

Croudace, I.W., and Rothwell, R.G. (Eds.), 2015. Micro-XRF Studies of Sediment Cores: Applications of a Non-destructive Tool for the Environmental Sciences: Dordrecht, Netherlands (Springer). **https://doi.org/10.1007/978-94-017-9849-5**

Dunlea, A.G., Murray, R.W., Tada, R., Alvarez-Zarikian, C.A., Anderson, C.H., Gilli, A., Giosan, L., Gorgas, T., Hennekam, R., Irino, T., Murayama, M., Peterson, L.C., Reichart, G.-J., Seki, A., Zheng, H., and Ziegler, M., 2020. Intercomparison of XRF core scanning results from seven labs and approaches to practical calibration. Geochemistry, Geophysics, Geosystems, 21(9):e2020GC009248. **https://doi.org/10.1029/2020GC009248**

Gäng, F., Böning, P., Brüchert, V., Lahajnar, N., and Pahnke, K., 2023. Critical assessment of U, Ba and Ni as redox and productivity proxies in organic-rich sediments underneath dynamic, highly productive waters. Geochimica et Cosmochimica Acta, 348:206–220. **https://doi.org/10.1016/j.gca.2023.03.015**

Grützner, J., Rebesco, M.A., Cooper, A.K., Forsberg, C.F., Kryc, K.A., and Wefer, G., 2003. Evidence for orbitally controlled size variations of the East Antarctic Ice Sheet during the late Miocene. Geology, 31(9):777–780. **https://doi.org/10.1130/G19574.1**

Jimenez-Espejo, F.J., Presti, M., Kuhn, G., McKay, R., Crosta, X., Escutia, C., Lucchi, R.G., Tolotti, R., Yoshimura, T., Ortega Huertas, M., Macrì, P., Caburlotto, A., and De Santis, L., 2020. Late Pleistocene oceanographic and depositional variations along the Wilkes Land margin (East Antarctica) reconstructed with geochemical proxies in deep-sea sediments. Global and Planetary Change, 184:103045. **https://doi.org/10.1016/j.gloplacha.2019.103045**

Kasuya, T., Iwasaki, S., and Okazaki, Y., 2023. Data report: calibration of XRF scanning $CaCO_3$ estimates for the upper 30 m along the Site U1543 splice, International Ocean Discovery Program Expedition 383. In Lamy, F., Winckler, G., Alvarez Zarikian, C.A., and the Expedition 383 Scientists, Dynamics of the Pacific Antarctic Circumpolar Current. Proceedings of the International Ocean Discovery Program, 383: College Station, TX (International Ocean Discovery Program). **https://doi.org/10.14379/iodp.proc.383.201.2023**

Kulhanek, D.K., Prunella, C., McLaughlin, J.R., Griffin, B., McKay, R.M., Patterson, M.O., Gales, J., Shevenell, A.E., van Peer, T.E., and the Expedition 374 Scientists, 2022. Data report: Site U1523 composite section and stratigraphic splice based on X-ray fluorescence data, IODP Expedition 374. In McKay, R.M., De Santis, L., Kulhanek, D.K., and the Expedition 374 Scientists, Ross Sea West Antarctic Ice Sheet History. Proceedings of the International Ocean Discovery Program, 374: College Station, TX (International Ocean Discovery Program). **https://doi.org/10.14379/iodp.proc.374.202.2022**

Lyle, M.W., Olivarez Lyle, A., Gorgas, T., Holbourn, A., Westerhold, T., Hathorne, E., Kimoto, K., and Yamamoto, S., 2012. Data report: raw and normalized elemental data along the Site U1338 splice from X-ray fluorescence scanning. In Pälike, H., Lyle, M., Nishi, H., Raffi, I., Gamage, K., Klaus, A., and the Expedition 320/321 Scientists, Proceeding of the Integrated Ocean Drilling Program, 320/321: Tokyo (Integrated Ocean Drilling Program Management International, Inc.). **https://doi.org/10.2204/iodp.proc.320321.203.2012**

Marschalek, J.W., Zurli, L., Talarico, F., van de Flierdt, T., Vermeesch, P., Carter, A., Beny, F., Bout-Roumazeilles, V., Sangiorgi, F., Hemming, S.R., Pérez, L.F., Colleoni, F., Prebble, J.G., van Peer, T.E., Perotti, M., Shevenell, A.E., Browne, I., Kulhanek, D.K., Levy, R., Harwood, D., Sullivan, N.B., Meyers, S.R., Griffith, E.M., Hillenbrand, C.D., Gasson, E., Siegert, M.J., Keisling, B., Licht, K.J., Kuhn, G., Dodd, J.P., Boshuis, C., De Santis, L., McKay, R.M., and the IODP Expedition 374 Scientists, 2021. A large West Antarctic Ice Sheet explains early Neogene sea-level amplitude. Nature, 600(7889):450–455. **https://doi.org/10.1038/s41586-021-04148-0**

McKay, R., Cockrell, J., Shevenell, A.E., Laberg, J.S., Burns, J., Patterson, M., Kim, S., Naish, T., Harwood, D., Levy, R., Marschalek, J., van de Flierdt, T., Ishino, S., Keisling, B., Sousa, I.M.C.d., Cortese, G., Sangiorgi, F., Leckie, R.M., Dodd, J., Duncan, B., Pérez, L.F., Romans, B.W., Kim, S., Bombard, S., Browne, I., van Peer, T., Seki, O., Colleoni, F., Kulhanek, D., De Santis, L., and the IODP Expedition 374 Science Team, 2024. Miocene ice sheet dynamics and sediment deposition in the central Ross Sea, Antarctica. Geological Society of America Bulletin, 137(3–4):1267–1291. **https://doi.org/10.1130/B37613.1**

McKay, R.M., De Santis, L., Kulhanek, D.K., Ash, J.L., Beny, F., Browne, I.M., Cortese, G., Cordeiro de Sousa, I.M., Dodd, J.P., Esper, O.M., Gales, J.A., Harwood, D.M., Ishino, S., Keisling, B.A., Kim, S., Kim, S., Laberg, J.S., Leckie, R.M., Müller, J., Patterson, M.O., Romans, B.W., Romero, O.E., Sangiorgi, F., Seki, O., Shevenell, A.E., Singh, S.M., Sugisaki, S.T., van de Flierdt, T., van Peer, T.E., Xiao, W., and Xiong, Z., 2019a. Expedition 374 summary. In McKay, R.M., De Santis, L., Kulhanek, D.K., and the Expedition 374 Scientists, Ross Sea West Antarctic Ice Sheet History. Proceedings of the International Ocean Discovery Program, 374: College Station, TX (International Ocean Discovery Program). **https://doi.org/10.14379/iodp.proc.374.101.2019**

McKay, R.M., De Santis, L., Kulhanek, D.K., Ash, J.L., Beny, F., Browne, I.M., Cortese, G., Cordeiro de Sousa, I.M., Dodd, J.P., Esper, O.M., Gales, J.A., Harwood, D.M., Ishino, S., Keisling, B.A., Kim, S., Kim, S., Laberg, J.S., Leckie, R.M., Müller, J., Patterson, M.O., Romans, B.W., Romero, O.E., Sangiorgi, F., Seki, O., Shevenell, A.E., Singh, S.M., Sugisaki, S.T., van de Flierdt, T., van Peer, T.E., Xiao, W., and Xiong, Z., 2019b. Site U1521. In McKay, R.M., De Santis, L., Kulhanek, D.K., and the Expedition 374 Scientists, Ross Sea West Antarctic Ice Sheet History. Proceedings of the International Ocean Discovery Program, 374: College Station, TX (International Ocean Discovery Program). **https://doi.org/10.14379/iodp.proc.374.103.2019**

Monien, D., Kuhn, G., von Eynatten, H., and Talarico, F.M., 2012. Geochemical provenance analysis of fine-grained sediment revealing Late Miocene to recent Paleo-Environmental changes in the Western Ross Sea, Antarctica. Global and Planetary Change, 96–97:41–58. **https://doi.org/10.1016/j.gloplacha.2010.05.001**

Patterson, M.O., McKay, R., Naish, T., Escutia, C., Jimenez-Espejo, F.J., Raymo, M.E., Meyers, S.R., Tauxe, L., Brinkhuis, H., Klaus, A., Fehr, A., Bendle, J.A.P., Bijl, P.K., Bohaty, S.M., Carr, S.A., Dunbar, R.B., Flores, J.A., Gonzalez, J.J., Hayden, T.G., Iwai, M., Katsuki, K., Kong, G.S., Nakai, M., Olney, M.P., Passchier, S., Pekar, S.F., Pross, J., Riesselman, C.R., Röhl, U., Sakai, T., Shrivastava, P.K., Stickley, C.E., Sugasaki, S., Tuo, S., van de Flierdt, T., Welsh, K., Williams, T., and Yamane, M., 2014. Orbital forcing of the East Antarctic ice sheet during the Pliocene and early Pleistocene. Nature Geoscience, 7(11):841–847. **https://doi.org/10.1038/ngeo2273**

Penkrot, M.L., Jaeger, J.M., Cowan, E.A., St-Onge, G., and LeVay, L., 2018. Multivariate modeling of glacimarine lithostratigraphy combining scanning XRF, multisensory core properties, and CT imagery: IODP Site U1419. Geosphere, 14(4):1935–1960. **https://doi.org/10.1130/GES01635.1**

Pérez, L.F., De Santis, L., McKay, R.M., Larter, R.D., Ash, J., Bart, P.J., Böhm, G., Brancatelli, G., Browne, I., Colleoni, F., Dodd, J.P., Geletti, R., Harwood, D.M., Kuhn, G., Sverre Laberg, J., Leckie, R.M., Levy, R.H., Marschalek, J., Mateo, Z., Naish, T.R., Sangiorgi, F., Shevenell, A.E., Sorlien, C.C., van de Flierdt, T., and the International Ocean Discovery Program Expedition 374 Scientists, 2022. Early and middle Miocene ice sheet dynamics in the Ross Sea: results from integrated core-log-seismic interpretation. Geological Society of America Bulletin, 134(1–2):348–370. **https://doi.org/10.1130/B35814.1**

R Core Team, 2024. R: A language and environment for statistical computing. R Foundation for Statistical Computing. **https://www.r-project.org/**

Robustelli Test, C., Amadori, C., Borrelli, C., Christeson, G., Estes, E., Guertin, L., Hertzberg, J., Kaplan, M.R., Koorapati, R.K., Lam, A.R., Lowery, C.M., McIntyre, A., Reece, J., Routledge, C.M., Standring, P., Sylvan, J.B., Thompson, M., Villa, A., Wang, Y., Wee, S.Y., Williams, T., Yeon, J., Teagle, D.A.H., Coggon, R.M., and the Expedition 390/393 Scientists, 2024. Data report: X-ray fluorescence scanning of sediment cores, IODP Expedition 390/393 Site U1559, South Atlantic Transect. In Coggon, R.M., Teagle, D.A.H., Sylvan, J.B., Reece, J., Estes, E.R., Williams, T.J., Christeson, G.L., and the Expedition 390/393 Scientists, South Atlantic Transect. Proceedings of the International Ocean Discovery Program, 390/393: College Station, TX (International Ocean Discovery Program). **https://doi.org/10.14379/iodp.proc.390393.204.2024**

Tjallingii, R., Röhl, U., Kölling, M., and Bickert, T., 2007. Influence of the water content on X-ray fluorescence core-scanning measurements in soft marine sediments. Geochemistry, Geophysics, Geosystems, 8(2):Q02004. **https://doi.org/10.1029/2006GC001393**

Wei, T., and Simko, V., 2024. R package 'corrplot': visualization of a correlation matrix. (Version 0.95). **https://github.com/taiyun/corrplot**

Wilson, D.J., Bertram, R.A., Needham, E.F., van de Flierdt, T., Welsh, K.J., McKay, R.M., Mazumder, A., Riesselman, C.R., Jimenez-Espejo, F.J., and Escutia, C., 2018. Ice loss from the East Antarctic Ice Sheet during late Pleistocene interglacials. Nature, 561(7723):383–386. **https://doi.org/10.1038/s41586-018-0501-8**

Ziegler, M., Jilbert, T., de Lange, G.J., Lourens, L.J., and Reichart, G.-J., 2008. Bromine counts from XRF scanning as an estimate of the marine organic carbon content of sediment cores. Geochemistry, Geophysics, Geosystems, 9(5). **https://doi.org/10.1029/2007GC001932**